



Significant Effects of Shallow Seismic and Stress Properties on Phase Velocities of Rayleigh Waves Up to 20 s

CHENHAO YANG,¹ GUOLIANG LI,^{1,2} FENGLIN NIU,^{1,2} and YEHUDA BEN-ZION³

Abstract—Seismic data are increasingly used to monitor sub-surface velocity changes associated with tectonic and environmental processes that occur in different depth sections. To clarify the differences between effects associated with shallow and deep changes of properties, we conduct numerical experiments using simple layered models that include low velocities, low attenuation coefficients and stress-sensitivity of cracked rocks in the shallow crust. We find significant phase-velocity drops in the period range of 5–20 s when large structural changes occur in the top 1–3 km. The apparent velocity changes ($\delta v/v$) measured from the first part of the synthetic Rayleigh waves with a cross-correlation based technique show significant velocity drops in the period bands of 5–10 s and 10–20 s that are consistent with reported values of changes at seismogenic depth. The results highlight the importance of accounting for low velocities, attenuation coefficients and stress-sensitivity of parameters in the top 1–3 km in studies aiming to determine the source region of temporal changes. Analyses using different frequency ranges and calculations of apparent delay times over multiple period bands are essential for resolving the depth range of temporal changes of properties. For temporal changes occurring at seismogenic depths, the measured $\delta v/v$ values at 5–10 s are significantly larger than those of 10–20 s, which are not observed for shallow changes.

Key words: Time-lapse seismic imaging, temporal changes in seismic structure, coseismic stress drop, shallow structural damage, Rayleigh wave phase velocity, apparent velocity change.

1. Introduction

Recent advances in seismic data acquisition and computational power have led to significant progress

in time-lapse (4-D) seismic imaging. A growing number of studies report on temporal changes of seismic velocities associated with the occurrence of earthquakes (e.g., Schaff and Beroza 2004; Peng and Ben-Zion 2006; Sawazaki et al. 2009), volcanic deformation (e.g., Sens-Schönfelder and Wegler, 2006; Brenguier et al. 2008), and various non-tectonic processes such as precipitation, thermoelastic strain and changes of water level in reservoirs (e.g., Meier et al. 2010; Chen et al. 2014; Hillers et al. 2015; Lecocq et al. 2017). The techniques used to monitor temporal changes of seismic properties are associated with different types of data and analysis time steps. Studies using earthquake waveforms are associated mainly with body and coda waves, and have time resolution that can approach in cases involving aftershock sequences of minutes to seconds. Several such studies reported on co-seismic temporal changes of velocities with amplitudes of a few percent to tens of percent (e.g., Rubinstein and Beroza 2005; Wu et al. 2009; Zhao and Peng 2009; Nakata and Snieder 2011; Roux and Ben-Zion 2014), and concluded from borehole observations and modeling that the changes occur primarily in the top few hundred meters of the crust.

Using the ambient seismic noise to monitor temporal changes has become a significant technique with many applications (e.g., Brenguier et al. 2008, 2014; Cheng et al. 2010; Sens-Schönfelder and Larose 2010; Obermann et al. 2014). These studies use typically Rayleigh waves and time steps of days or more, since stacking is required to increase the signal-to-noise ratio of the waves that are extracted from the noise correlations. The amplitudes of temporal changes reported by noise-based studies are typically a fraction of a percent, and the depth section

¹ Department of Earth, Environmental and Planetary Sciences, Rice University, 6100 Main St, Houston, TX 77005, USA. E-mail: niu@rice.edu

² State Key Laboratory of Petroleum Resource and Prospecting, and Unconventional Gas Institute, China University of Petroleum at Beijing, Beijing 102249, China.

³ Department of Earth Sciences, University of Southern California, Los Angeles, CA 90089-0740, USA.

sustaining the changes is inferred from the used frequency band. For example, Cheng et al. (2010) observed $\sim 0.4\%$ temporal changes of seismic velocities after the 2008 M_w 7.9 Wenchuan earthquake in China. The analysis employed 10–25 s Rayleigh waves, leading to inferred depth sustaining the changes up to 25 km. Froment et al. (2013) observed similar changes following the M_w 7.9 Wenchuan event using both 1–3 s and 12–20 s Rayleigh waves, and interpreted the results as reflecting deformation that extends to seismogenic depth. Rivet et al. (2011) found $\sim 0.1\%$ temporal changes of seismic velocities following a slow slip event in the Guerrero region, Mexico, with periods ranging from 4 s to over 25 s. The changes were largest for 7–17 s Rayleigh waves, leading to inferred depth range of 5–20 km. Brenguier et al. (2014) observed ~ 0.01 – 0.1% velocity reductions across Japan following the 2011 M_w 9.0 Tohoku-Oki earthquake, with the most significant changes beneath Quaternary volcanoes. The analysis used Rayleigh waves with frequencies around 0.1–0.9 Hz, and the changes were attributed to a depth range between the surface and 10 km.

Clearly, resolving the depth range sustaining temporal changes of seismic properties requires analysis over different frequency ranges. Obermann et al. (2013) investigated with numerical experiments the depth sensitivity of high-frequency surface and coda waves to velocity perturbations, and found that the shallow structure can have a significant influence on the wavefield. In the present study we analyze with numerical simulations the sensitivity of intermediate-frequency Rayleigh waves to velocity, attenuation and stress changes at various depth sections of crustal structures. The analysis includes computing apparent velocity changes $\delta v/v$ with a technique based on cross-correlation of the first part of Rayleigh waves in different frequency bands. Significant changes of both phase and apparent velocities at periods up to 20 s are found in some cases with changes of properties limited to the top 1–3 km (i.e., above the seismogenic zone). Comparisons of the relative phase and apparent velocity changes observed using different frequency ranges can help to resolve the depth section where the temporal changes occur.

2. Numerical Modeling

2.1. Model Settings

We first set a reference 1-D layered model for the numerical simulations with constant mass density, seismic velocity and attenuation quality factor in each layer. As many studies of temporal changes are based on seismic stations located in sedimentary basins, we include 3.5 km thick sediments in the model. The model consists of four sedimentary layers, two crystalline crustal layers and an underlying half-space substrate (Fig. 1; Table 1). We refer to this model as the original model in the rest of the paper. To investigate how structural and stress perturbations

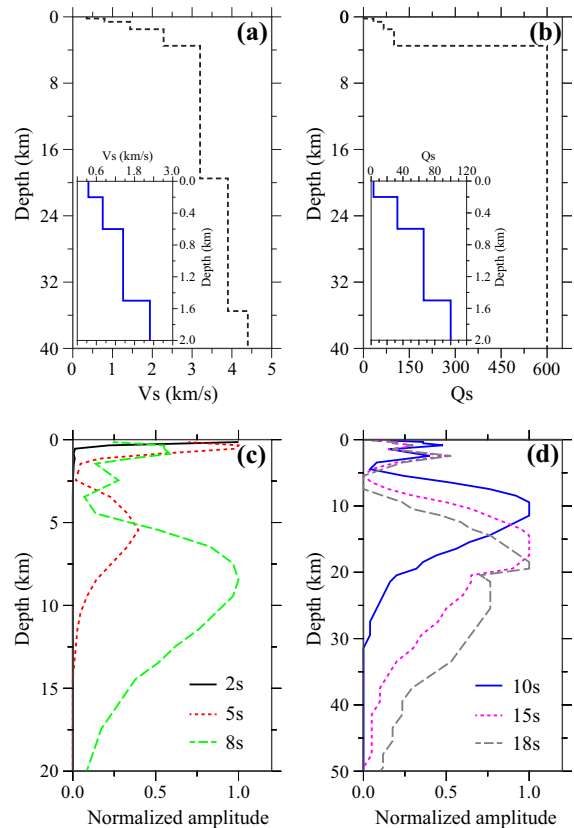


Figure 1

S-wave velocity and Q_s of the original model are shown in dashed lines in **a**, **b**, respectively. Blue insets show the top 2 km of the velocity and attenuation structure. **c** Phase velocity sensitivity kernels of 2 s (black solid line), 5 s (red dotted line), and 8 s (green dashed line) Rayleigh waves are plotted in the depth range of 0–20 km. **d** is similar to **c** except for 10 s (blue solid line), 15 s (purple dotted line), and 18 s (grey dashed line) Rayleigh waves, and the depth range, which is 0–50 km

Table 1
Parameters of the initial model for case 1

H^a (km)	α (km/s)	β (km/s)	ρ (g/cm ³)	Qs
0.2	1.50	0.35	1.93	3.0
0.4	2.22	0.80	2.12	33.0
0.9	2.88	1.44	2.25	66.0
2.0	4.57	2.28	2.52	100.0
16.0	5.80	3.20	2.60	600.0
16.0	6.80	3.90	2.90	600.0
80.0	8.02	4.40	3.38	600.0

^aThickness of each layer

affect the velocity of Rayleigh waves at the surface, we generate 12 models by changing some parts of the original model. We divide these cases into four categories summarized in Table 2. Categories 1 and 2 with eight models are designed to investigate effects associated with changes occurring in sediments shallower than 1.5 km, model 9 in category 3 is used to probe effects involving perturbations at seismogenic depth, and five additional models in category 4 to investigate stress-induced velocity changes.

The four cases in category 1 incorporate changes of velocity and density, whereas those in category 2 have additional changes of attenuation. A 30%

reduction of seismic velocity in the shallow sediments is assumed in models 1–8, in agreement with large coseismic drops observed by studies using earthquake waveforms and very short time sampling (e.g., Karabulut and Bouchon 2007; Wu et al. 2009). A 5% velocity reduction over the depth section 5–10 km in model 9 is an upper bound to the inferred observational values. We expect that large coseismic stress drops within seismogenic zones can cause significant changes in seismic velocity. Velocity drops in models 10 and 11 are computed with a velocity-stress sensitivity coefficient ($\delta \ln V / \delta p$) based on laboratory experiments of Nur and Simmons

Table 2
Parameters of the initial model for case 1

Cat.	Model	Dep. range (km)		Vel. change (%)		Q change (%)		$\delta v/v$ (%)	
		Top	Bottom	Top	Bottom	Top	Bottom	5–10 s	10–20 s
1	1	0.00	0.60	30.00	30.00	0.0	0.0	– 0.32	– 0.51
	2	0.00	0.60	30.00	0.00	0.0	0.0	– 0.42	– 0.49
	3	0.00	1.50	30.00	30.00	0.0	0.0	– 1.34	– 1.27
	4	0.00	1.50	30.00	0.00	0.0	0.0	– 0.69	– 0.73
2	5	0.00	0.60	30.00	30.00	30.0	30.0	– 0.31	– 0.50
	6	0.00	0.60	30.00	0.00	30.0	0.0	– 0.41	– 0.49
	7	0.00	1.50	30.00	30.00	30.0	30.0	– 1.34	– 1.27
	8	0.00	1.50	30.00	0.00	30.0	0.0	– 0.68	– 0.73
3	9	5.00	10.00	5.0	5.00	0.0	0.0	– 2.98	– 1.84
4	10 ^a	0.00	3.34	9.40	0.06	0.0	0.0	– 0.05	– 0.03
	11 ^a	0.00	3.34	28.19	0.18	0.0	0.0	– 0.08	– 0.09
	12	0.00	3.00	30.0	5.00	0.0	0.0	– 2.01	– 1.63
	13	0.00	3.00	10.0	5.00	0.0	0.0	– 1.04	– 0.85
	14	0.00	3.00	5.0	5.00	0.0	0.0	– 0.74	– 0.64

^aVelocity drops of models 10 and 11 are computed with laboratory velocity-stress sensitivity data of Nur and Simmons (1969) listed in Table 3 with a stress drop of 10 MPa and 30 MPa, respectively

Table 3

Velocity–stress sensitivity of Nur and Simmons (1969)

Pressure (Kbar)	Depth (km)	$d\ln V/dp$ (10^{-8} Pa^{-1})
0.017	0.06	9.399
0.039	0.13	6.285
0.059	0.20	5.047
0.077	0.26	1.183
0.142	0.47	0.710
0.195	0.65	0.543
0.250	0.83	0.473
0.288	0.96	0.304
0.346	1.15	0.205
0.416	1.39	0.167
0.555	1.85	0.128
0.683	2.28	0.063
1.001	3.34	0.063

(1969) using stress drops of 10 MPa and 30 MPa, respectively. Model 12 has a velocity-stress sensitivity based on field observations (Niu et al. 2008, and references therein) and a stress drop of 10 MPa. Details of $\delta\ln V/\delta p$ are shown in Table 3.

The physical basis for the stress sensitivity of seismic velocity in the crust is the presence of cracks in the rocks. Their effect on seismic velocity on the one hand, and their sensitivity to the ambient stress field on the other, means that seismic velocities in cracked rocks are generally stress sensitive (e.g., Lyakhovskiy et al. 1997; Hamiel et al. 2009) and depend on the presence of fluids. The measured stress sensitivity of dry rock samples in the lab is of the order of 10^{-7} Pa^{-1} at atmospheric pressure and decreases rapidly to 10^{-10} – 10^{-9} Pa^{-1} at a pressure of ~ 100 MPa. With a stress drop of 10 MPa, model 10 has a velocity reduction of $\sim 10\%$ at the surface that decreases rapidly to $\sim 0.06\%$ around 3 km depth. These changes are tripled in model 11, which has a stress drop of 30 MPa. Field measurements of $\delta\ln V/\delta p$ are more scattered than laboratory results and range from 10^{-9} to 10^{-6} Pa^{-1} near the surface (e.g., Yamamura et al. 2003, Silver et al. 2007). Niu et al. (2008) measured velocity perturbations at a depth of ~ 1 km in the SAFOD drill site near Parkfield, California, and found stress sensitivity of $\sim 10^{-7} \text{ Pa}^{-1}$, which is approximately two orders of magnitude larger than the results of Nur and Simmons (1969) for corresponding confining pressure. These studies suggest that the in situ stress

sensitivity at depth could be larger than lab measurements due to pervasive heterogeneities and fluids. Therefore, we construct model 12 that has a velocity drop of 30% at the surface and decreases linearly to 5% at 3 km depth, considering the field measurements of the $\delta\ln V/\delta p$ and depth variable stress changes. For comparison, we also construct two more models (model 13 and model 14), which have a velocity drop of 10% and 5% at the surface and change linearly to 5% at 3 km depth.

For each of the 15 models (one original + 14 perturbed models), we compute the phase velocity in the period range of 2 to 20 s, the corresponding sensitivity kernels of the phase velocities, and the Rayleigh wave Green's functions. A cross-correlation based method is used to estimate the apparent velocity changes in the period bands of 5–10 s and 10–20 s for the 15 perturbed models.

2.2. Calculation of Rayleigh Wave Phase Velocities

The Thomson-Haskell propagator matrix is used to compute Rayleigh waves in a 1-D structure consisting of a stack of constant velocity layers on top of a half space. The displacement-stress field observed at the surface is linked to those at the top of the half space by the product of the propagator matrices of each layer. The stress-free boundary condition is applied to the surface, and displacements are set to zero at the bottom of the half space, which is implemented by allowing only downgoing P and SV waves within the half spaces. This results in the following equation:

$$\begin{pmatrix} p_{n+1}(z_n) \\ s_{n+1}(z_n) \\ 0 \\ 0 \end{pmatrix} = \begin{pmatrix} B_{11} & B_{12} & B_{13} & B_{14} \\ B_{21} & B_{22} & B_{23} & B_{24} \\ B_{31} & B_{32} & B_{33} & B_{34} \\ B_{41} & B_{42} & B_{43} & B_{44} \end{pmatrix} \begin{pmatrix} r_1(z_0) \\ r_2(z_0) \\ 0 \\ 0 \end{pmatrix}. \quad (1)$$

Here, $r_1(z_0)$ and $r_2(z_0)$ are vertical and radial displacements at the surface, and p_{n+1} and s_{n+1} are the amplitudes of the downgoing P- and SV-waves. The B matrix is the product of the propagator matrices, which can be computed from the P, S wave velocities and density for given angular frequency ω and wavenumber k . The eigenvalue k and eigenvector

$((r_1(z_0), r_1(z_0))^T$ can be determined from the zero-determinant of the submatrix B:

$$\begin{vmatrix} B_{31} & B_{32} \\ B_{41} & B_{42} \end{vmatrix} = 0. \tag{2}$$

To find the root of this determinant for a given ω , a series of trial values of k are tested until (2) is met. This method provides the dispersion curves of a given layered elastic model.

To compute the phase velocities in an anelastic medium with attenuation coefficients Q_p and Q_s , one can simply replace the frequency independent elastic P- and S-wave velocities (α_e and β_e) with frequency dependent complex velocities (α_a and β_a) in the propagator matrix of each layer (Liu et al. 1976):

$$\begin{aligned} \alpha_e \rightarrow \alpha_a &= \alpha(\omega) \left(1 + \frac{i}{2Q_p(\omega)} \right) \\ &= \alpha(\omega_0) \left(1 + \frac{1}{\pi Q_p} \log \frac{\omega}{\omega_0} + \frac{i}{2Q_p} \right) \\ \beta_e \rightarrow \beta_a &= \beta(\omega) \left(1 + \frac{i}{2Q_s(\omega)} \right) \\ &= \beta(\omega_0) \left(1 + \frac{1}{\pi Q_s} \log \frac{\omega}{\omega_0} + \frac{i}{2Q_s} \right) \end{aligned} \tag{3}$$

Here, ω_0 is a reference angular frequency set to 2π , equivalent to a reference frequency of 1 Hz.

The anelastic phase velocities can also be computed from perturbation theory. If we treat the complex velocities as adding to the elastic velocities with the following small perturbations:

$$\begin{aligned} \delta\alpha &= \alpha_a - \alpha(\omega_0) = \frac{\alpha(\omega_0)}{Q_p} \left(\frac{1}{\pi} \ln \frac{\omega}{\omega_0} + \frac{i}{2} \right) \\ \delta\beta &= \beta_a - \beta(\omega_0) = \frac{\beta(\omega_0)}{Q_s} \left(\frac{1}{\pi} \ln \frac{\omega}{\omega_0} + \frac{i}{2} \right), \end{aligned} \tag{4}$$

then the phase velocities in anelastic media can be written as:

$$c_a(\omega) = c_e(\omega) + \delta c(\omega). \tag{5}$$

Here, the phase-velocity perturbations, $\delta c(\omega)$, can be computed from

$$\delta c(\omega) = \left(\frac{1}{\pi} \ln \frac{\omega}{\omega_0} + \frac{i}{2} \right) \cdot \int_0^\infty \left[\frac{\alpha(z)}{Q_p(z)} \frac{\partial c}{\partial \alpha} + \frac{\beta(z)}{Q_s(z)} \frac{\partial c}{\partial \beta} \right] dz. \tag{6}$$

Since $\delta c(\omega)$ are complex functions, the phase velocities in anelastic media have complex values. In the results section we take the real parts as the phase velocities.

2.3. Calculation of Phase Velocity Sensitivity Kernels

In order to compute the sensitivity kernel of a Rayleigh wave phase velocity with respect to S-wave velocity at a fixed frequency ω_0 , we first increase the S velocity of a given model by 1% at depth z , and then calculate the phase velocity difference between the given and perturbed models. The ratio of the relative phase velocity change and the S velocity perturbation, $d \ln c(\omega_0)/d \ln \beta(z)$, is the sensitivity at depth z . Varying z over the depth range provides the phase velocity sensitivity kernel at frequency ω_0 .

2.4. Green's functions of the fundamental Rayleigh wave

A wave packet with a given spectral density $A(\omega)$ and initial phase $\phi_0(\omega)$ composed of a single mode can be expressed as:

$$f(r, t) = \frac{1}{2\pi\sqrt{r}} \int_{-\infty}^{+\infty} A(\omega) e^{-i\omega \left(t - \frac{r}{c_a(\omega)} \right) + i\phi_0(\omega)} d\omega. \tag{7}$$

Here, $r^{-1/2}$ accounts for geometrical spreading and $c_a(\omega)$ is the complex phase velocity in anelastic media. For an impulse source, $A(\omega) = 1$ and $\phi_0(\omega) = 0$. Thus the Green's functions of the fundamental mode Rayleigh wave at epicentral distance r can be computed by:

$$f(r, t) = \frac{1}{2\pi\sqrt{r}} \int_{-\infty}^{+\infty} e^{-i\omega \left(t - \frac{r}{c_a(\omega)} \right)} d\omega. \tag{8}$$

2.5. Calculation of Apparent Velocity Change $\delta v/v$

We first bandpass-filter the Green's functions of the original model and the 12 perturbed models in two period bands, 5–10 s and 10–20 s. In each period band, we use the original Green's function as the reference trace and compute the cross-correlation functions of the Green's functions of the 12 models. Each cross-correlation is computed in time domain and a cosine function fitting is employed to obtain sub-sample delay times τ (Cespedes et al. 1995). We choose the first 10 s of the Rayleigh wave time window to highlight apparent velocity changes of the long-wavelength and, therefore, deeply penetrated surface waves. Finally, we divide the measured delay times by the arrival times T of the central point of the time window to obtain the apparent velocity drops, i.e., $\delta v/v = -\tau/T$.

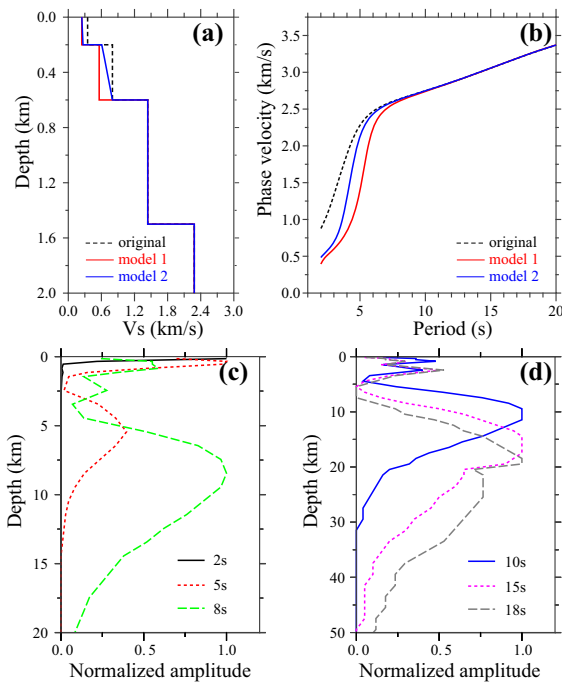


Figure 2

a S-wave velocity of model 1 (red solid line) and model 2 (blue solid line) are shown together with the original model (black dashed line). Only the top 2 km of the models is shown here. Model 1 has a constant 30% velocity drop in the top two layers from the origin model, while model 2 has a velocity drop of 30% at the surface, which decays gradually to zero at 0.6 km deep. **b** The phase velocity dispersion curves of the three model in the period range of 2–20 s. **c, d** Are similar to **c, d** in Fig. 1, except that they are computed with model 1

3. Results

Figure 1c, d display, respectively, the sensitivity kernels of the original model at periods 2 s, 5 s, 8 s, and 10 s, 15 s, 18 s. Note that different depth ranges are used in plotting the kernels of the two groups. All the kernels indicate that short to medium periods Rayleigh waves have significant sensitivity to structures shallower than 5 km. Therefore, large velocity perturbations at shallow depth may lead to significant changes of phase velocities at these periods. We illustrate this below by the 13 models with shallow structural changes that are limited to the top 3 km.

In model 1, we impose 30% drops of the P- and S-wave velocities as well as mass density, but not the quality factors. The reductions are limited to the two top sedimentary layers with a thickness of 0.6 km (Table 2, red solid line in Fig. 2a). Related milder changes are incorporated in model 2, where the reductions decrease linearly from 30% at the surface to 0% at the bottom of the second sedimentary layer (Table 2, blue solid line in Fig. 2a). The phase velocities of these two models are shown in Fig. 2b

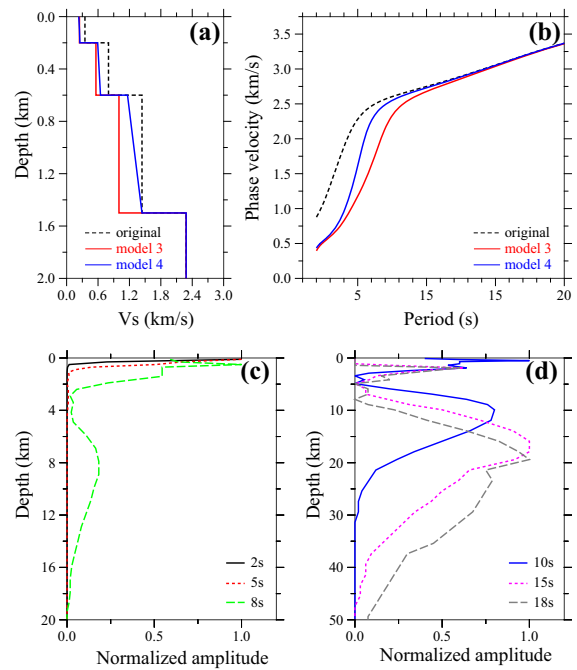


Figure 3

Results from model 3 and model 4. Same as Fig. 2, except that model 3 and model 4 are shown here, and the phase velocity kernels are computed with model 3

by red and blue solid lines, together with those from the original model (black dashed line). It is clear that the phase velocities calculated in the period range of 2-8 s of the two models are significantly lower than those computed from the original model. Figure 2c, d present the sensitivity kernels for models 1 and 2. The results are generally similar to those of the original model.

In model 3 we extend the 30% drops to the third sedimentary layer extending to 1.5 km below the surface, and in model 4 the reduction of properties decays from 30% at the top to 0% at 1.5 km depth. The two models and their corresponding phase velocities are shown (along with the dispersion curve of the original model) in Fig. 3a, b, respectively. Because of the additional velocity and density perturbation in the third sedimentary layer, the phase-velocity reduction of these two models is more significant and the effects on the dispersion curves extend to almost 12 s. The sensitive depth ranges of

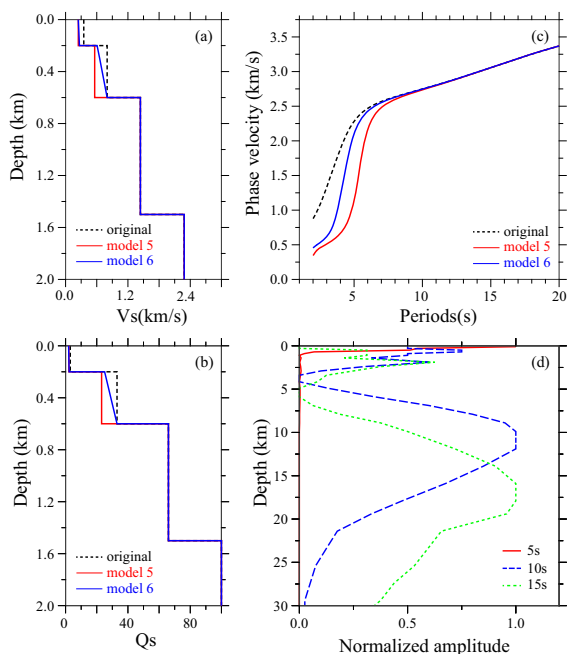


Figure 4

S-wave velocity and Q_s of model 5 and model 6 are shown with the original model in **a**, **b**, respectively. Only the top 2 km of the models are shown here. **c** The phase velocity dispersion curves of the three models in the period range of 2–20 s. **d** Phase velocity sensitivity kernels of 5 s (red solid line), 10 s (blue dashed line), and 15 s (green dotted line) Rayleigh waves computed from model 5 are plotted in the depth range of 0–30 km

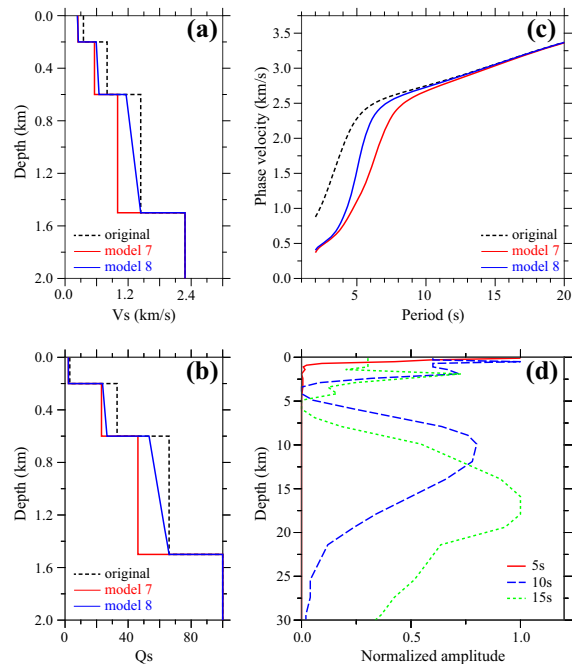


Figure 5

Results from model 7 and model 8. Same as Fig. 4, except that model 7 and model 8 are shown here, and the phase velocity kernels are computed with model 7

the three short periods (2 s, 5 s, and 8 s) also shift significantly to shallower values (Fig. 3c).

The four models in category 2 have the same velocity and density drops as in category 1, while also incorporating similar reduction of the S-wave quality factor. The four models and their corresponding phase velocities are shown in Figs. 4 and 5, respectively. All four models show significant phase velocity drops compared to the original model. The amount of observed drops are similar to their counterpart models in the category 1, suggesting that attenuation change plays a less important role than velocity and density perturbations in affecting properties of the Rayleigh waves. However, a changing attenuation quality factor can affect inferences on velocity structure by modifying the observable range of periods.

To investigate how velocity and density drops at seismogenic depth influence Rayleigh wave speed, we use model 9 with a 5% drop in P- and S-wave velocities and mass density in the depth range 5–10 km (Table 2, Fig. 6a). The attenuation structure is kept unchanged. The corresponding phase velocity

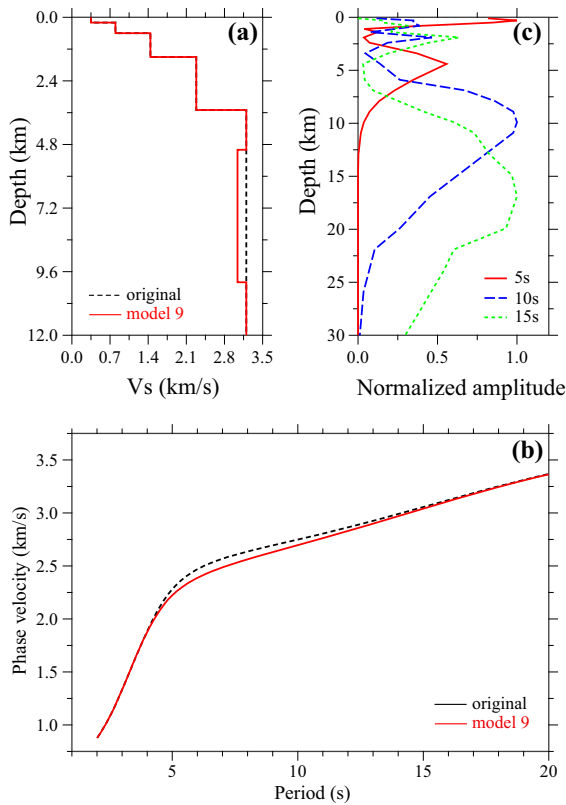


Figure 6

a S-wave velocity of model 9 (red solid line) is shown together with the original model (black dashed line). The model has a constant velocity drop of 5% in the depth range of 5–10 km. **b** Phase velocities of the model 9 and the original model are plotted as functions of period from 2 to 20 s. **c** Phase velocity sensitivity kernel of 5 s (red solid line), 10 s (blue dashed line), and 15 s (green dotted line) Rayleigh waves computed from model 9 (red solid line) are plotted in the depth range of 0–30 km

dispersion curve is shown in a red solid line in Fig. 6b, together with the original dispersion curve (black dashed line). The results show phase-velocity drops of a few percent in the period range ~ 4 –15 s (Fig. 6b). The sensitivity kernel of the 8 s phase velocity also changes slightly (Fig. 6c).

The five stress-related models in category 4 are associated with a velocity drop that extends to 3 km deep (Fig. 7a, b). This is considerably deeper than in the first eight models but still shallower than the seismogenic depth range in model 9. The attenuation structure of the five models is not changed. The calculated phase velocities of models 11 and 12 are shown in Fig. 7c with blue and red solid lines, respectively, along with the original dispersion curve

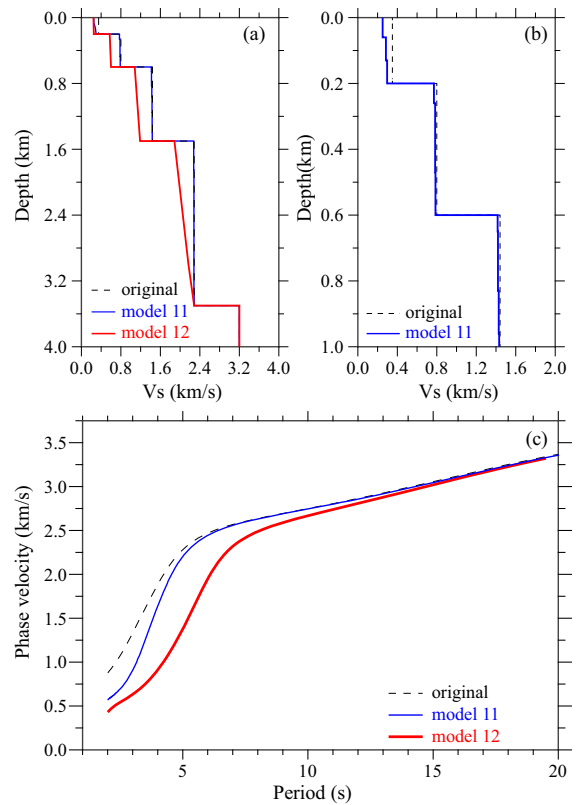


Figure 7

a S-wave velocities of model 11 (blue solid line) and 12 (red solid line) are shown together with the original model (black dashed line). The three models have the same velocity structure below ~ 3 km. **b** Shows a comparison of model 11 and the original model of the top 1 km where most of the velocity changes occur. **c** Phase velocities of model 11 (blue solid line) and 12 (red solid line) are plotted as functions of period from 2 to 20 s. The phase velocity dispersion curve of the original model (black dashed line) is also shown for comparison

(black dashed line). The differences in phase velocity between the two stress-related models and the original model are quite large at short periods and decrease gradually with increasing periods.

For comparison, we further show the calculated percentile phase velocity drops of the 14 models in Fig. 8. The left panels show changes of the 14 models in the period range of 2–20 s, while the right panels focus on changes in the period band of 15–20 s. Model 7 and model 12 in category 4 exhibit a phase velocity drop greater than 0.5% at a period of 20 s. This is comparable to the inferred co-seismic velocity changes reported for the 2004 M_w 6.6 Mid-Niigata earthquake (Wegler and Sens-Schönfelder 2007) and

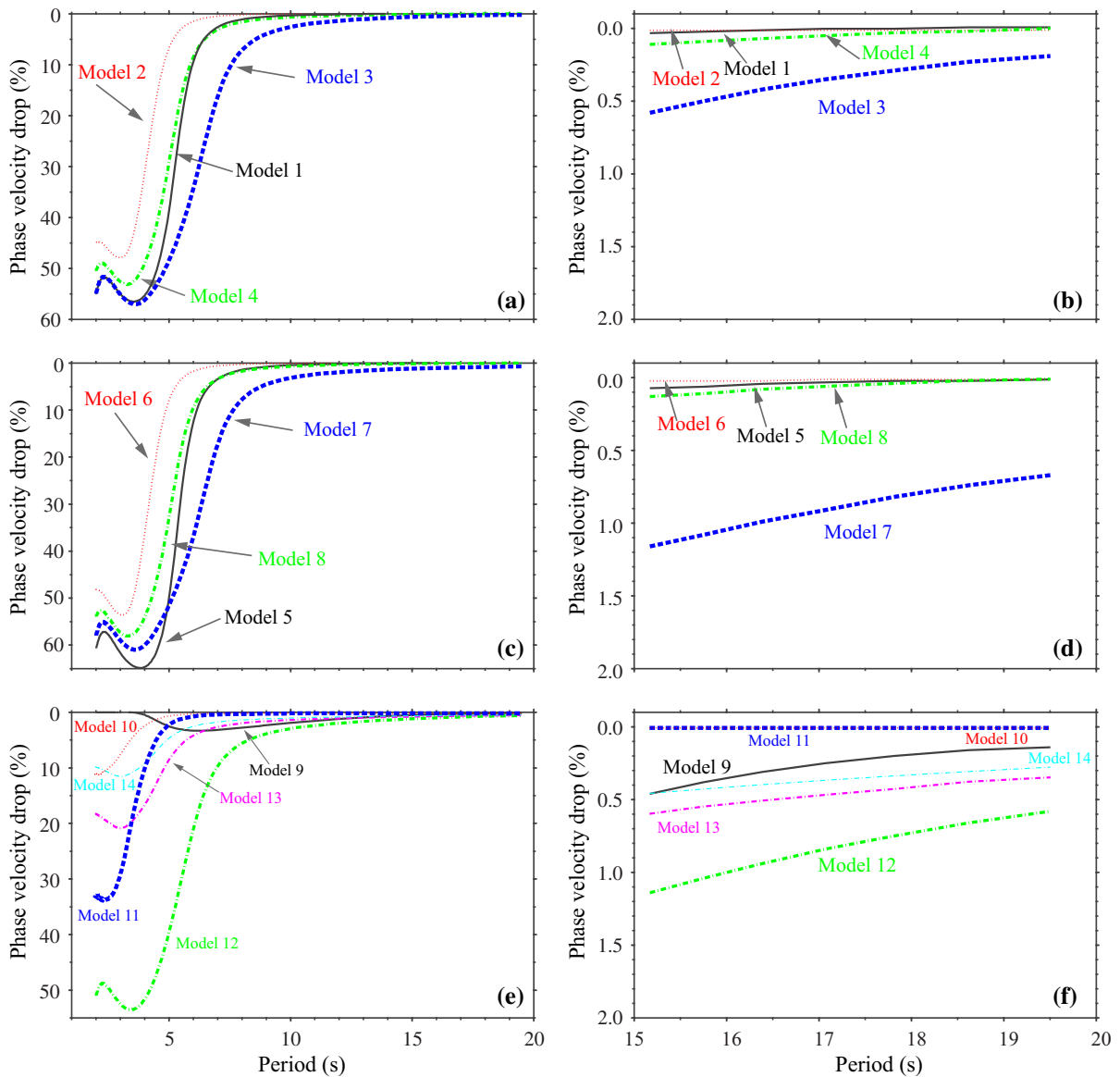


Figure 8

Phase velocity drops of models 1–4 are shown in the period band of 2–20 s (a) and 15–20 s (b), respectively. c, d Are similar to a, b except for models 5–8. e, f Are similar to a, b except for models 9–14

the 2008 M_w 7.9 Wenchuan earthquake (Cheng et al. 2010). Among the 14 perturbed models, only model 9 with a temporal change occurring at seismogenic depths shows a phase velocity reduction peaked at a period greater than 5 s. Model 9 is also featured by a slower decrease against increasing periods as compared to other models.

Figure 9 shows the filtered Green's functions of the 14 models in two period bands (5–10 s and 10–20 s) and measured apparent velocity changes, which are also listed in Table 2. Among the 14 examined cases, the measured apparent velocity changes of the first two stress-related models (models 10 and 11) are less than 0.1%. Seven models (models 1, 2, 4, 5, 6, 8, 14) show an apparent velocity drop in

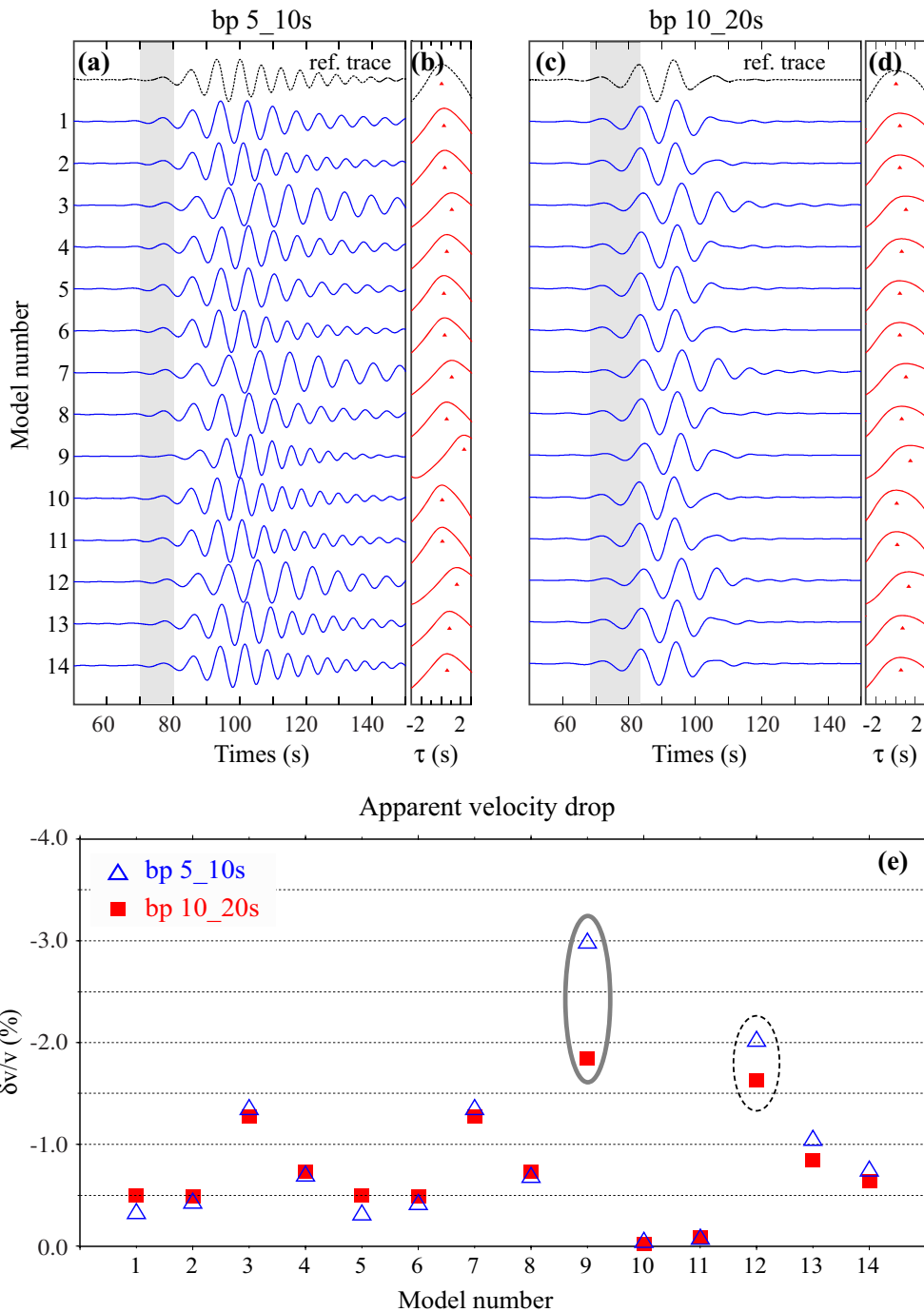


Figure 9

Rayleigh wave Green's functions computed from the original model and the 14 models with various types of structural changes are shown in grey and blue, respectively. The data are filtered in the period band from 5 to 10 s. **b** Shows the cross-correlation (cc) functions calculated between the Green's function of each model and the grey reference trace. The red dots indicate the peak of the cc functions. **c, d** Are similar to **a, b** except that the filtered period band is from 10 to 20 s. **e** The measured apparent velocity changes of the 14 models are shown in blue open triangles and red solid squares for the period bands of 5–10 s and 10–20 s, respectively. Note the large differences in the measurements of models 9 and 12, which are marked with grey solid and black dashed ellipses, respectively

the range of 0.3-1.0%. Models 3, 7, 9, 12 and 13 exhibit a velocity change of more than 1% (Fig. 9e; Table 2). The apparent velocity drops measured at the two period bands are generally comparable, other than for models 9 and 12 (the solid and dashed line ellipses in Fig. 9e; Table 2). The apparent velocity drops of the two models measured at the shorter period band 5–10 s (open triangles in Fig. 9e) are significantly larger than those measured at the longer period band 10–20 s (solid squares in Fig. 9e). It seems that the amount of difference in the measured apparent velocity drops between the two period bands is mostly sensitive to changes at deep parts of the media.

4. Discussion and Conclusions

We conduct numerical simulations to investigate how shallow structural and stress properties affect Rayleigh wave phase velocities in the period range 5–20 s, and to clarify the types of analysis needed to separate temporal changes limited to the shallow crust from those occurring in seismogenic zones. Calculations of sensitivity kernels and measurements of apparent velocity changes of Rayleigh waves in different frequency ranges show clearly the following results: (1) Phase velocities and sensitivity kernels of Rayleigh waves at periods up to 20 s can be affected significantly by the velocity structure in the top few kilometers of the crust. (2) Large velocity drops at shallow depth that may be caused by strong shaking of large earthquakes, with values consistent with those observed in some studies (e.g., Wu et al. 2009; Bonilla et al. 2018), can significantly affect Rayleigh wave phase velocities at periods up to 20 s. (3) Large velocity drops within the shallow sediments can produce $\sim 0.5\%$ apparent velocity changes even in analysis of temporal changes using 10–20 s Rayleigh wave data. (4) Stress changes in the top 3 km of the crust can produce considerable velocity changes that have significant effects on 10–20 s Rayleigh wave data.

The results highlight the importance of accounting for low velocities, attenuation coefficients and stress changes in the shallow crust in analyses of sensitivity kernels of Rayleigh waves, and in efforts

to determine the depth range sustaining temporal changes of seismic properties. Comparisons of the relative amplitudes of apparent velocity changes observed using different frequency ranges (e.g., Rivet et al. 2011; Liu et al. 2014; Obermann et al. 2014; Wu et al. 2016) are essential for separating effects limited to the very shallow structure from those occurring at greater depth. The apparent velocity changes measured from the first part of Rayleigh waves at the 10–20 s period band are significantly lower than those of the 5–10 s band for model 9 with changes at seismogenic depth (solid ellipse in Fig. 9e). This is in contrast to models 1–8 with velocity drops in the top 0.6 and 1.5 km. However, model 12 with stress-related coseismic velocity changes in the top ~ 3 km of the crust produces apparent velocity changes that are comparable to model 9 with velocity drop in the depth range 5–10 km (dashed ellipse in Fig. 9e).

The results of the present paper can be strengthened by performing similar calculations in 3-D models that incorporate lateral variations of properties in addition to the depth-dependent changes assumed here. Simulations using 3-D velocity models with the presence of randomly distributed scatterers are particularly important, as many lag time measurements are based on the coda wavefield (e.g., Brenguier et al. 2008, 2014; Obermann et al. 2014, 2016, 2018). Such calculations are computationally very intensive but should be attempted in follow-up works.

Acknowledgements

All figures are made using the Generic Mapping Tools (www.gmt.soest.hawaii.edu; Wessel et al. 2013). We thank Dr. Anne Obermann and another anonymous reviewer for their constructive comments and suggestions, which significantly improved the quality of this paper. C.Y. and F.N. were supported by NSF (Grant EAR-1251667) and G.L. was funded by NSFC (Grant 41630209). Y.B.Z. acknowledges support by the Wiess visiting professorship program of Rice University and the Department of Energy (award DESC0016520).

Publisher's Note Springer Nature remains neutral with regard to jurisdictional claims in published maps and institutional affiliations.

REFERENCES

- Bonilla, L. F., Guéguen, P., Ben-Zion, Y. (2018). Monitoring coseismic temporal changes of shallow material during strong ground motion with interferometry and autocorrelation, *Bulletin of the Seismological Society of America*, in press.
- Brenguier, F., Campillo, M., Takeda, T., Aoki, Y., Shapiro, N. M., Briand, X., et al. (2014). Mapping pressurized volcanic fluids from induced crustal seismic velocity drops. *Science*, *345*, 80–82.
- Brenguier, F., Shapiro, N. M., Campillo, M., Ferrazzini, V., Duputel, Z., Coutant, O., et al. (2008). Towards forecasting volcanic eruptions using seismic noise. *Nature Geoscience*, *1*, 126–130. <https://doi.org/10.1038/ngeo104>.
- Cespedes, I., Huang, Y., Ophir, J., & Spratt, S. (1995). Methods for estimation of sub-sample time delays of digitized echo signals. *Ultrasonic Imaging*, *17*, 142–171.
- Chen, H., Ge, H., & Niu, F. (2014). Semiannual velocity variations around the 2008 M_w 7.9 Wenchuan Earthquake fault zone revealed by ambient noise and ACROSS active source data. *Earthquake Science*. <https://doi.org/10.1007/s11589-014-0089-5>.
- Cheng, X., Niu, F., & Wang, B. (2010). Coseismic velocity change in the rupture zone of the 2008 M_w 7.9 Wenchuan earthquake observed from ambient seismic noise data. *Bulletin of the Seismological Society of America*, *100*, 2539–2550. <https://doi.org/10.1785/0120090329>.
- Froment, B. M., Campillo, M., Chen, J. H., & Liu, Q. Y. (2013). Deformation at depth associated with the 12 May 2008 M_w 7.9 Wenchuan earthquake from seismic ambient noise monitoring. *Geophysical Research Letters*, *40*, 78–82. <https://doi.org/10.1029/2012GL053995>.
- Hamiel, Y., Lyakhovskiy, V., Stanchits, S., Dresen, G., & Ben-Zion, Y. (2009). Brittle deformation and damage-induced seismic wave anisotropy in rocks. *Geophysical Journal International*, *178*, 901–909. <https://doi.org/10.1111/j.1365-246X.2009.04200.x>.
- Hillers, G., Ben-Zion, Y., Campillo, M., & Zigone, D. (2015). Seasonal variations of seismic velocities in the San Jacinto Fault area observed with ambient seismic noise. *Geophysical Journal International*, *202*, 920–932. <https://doi.org/10.1093/gji/ggv151>.
- Karabulut, H., & Bouchon, M. (2007). Spatial variability and non-linearity of strong ground motion near a fault. *Geophysical Journal International*, *45*, 22–33. <https://doi.org/10.1111/j.1365-246X.2007.03406.x>.
- Lecocq, T., Longuevergne, L., Pedersen, H. A., Brenguier, F., & Stammler, K. (2017). Monitoring ground water storage at mesoscale using seismic noise: 30 years of continuous observation and thermo-elastic and hydrological modeling. *Scientific Reports*. <https://doi.org/10.1038/s41598-017-14468-9>.
- Liu, H.-P., Anderson, D. L., & Kanamori, H. (1976). Velocity dispersion due to anelasticity; implications for seismology and mantle composition. *Geophysical Journal International*, *47*(1), 41–58.
- Liu, Z., Huang, J., Peng, Z., & Su, J. (2014). Seismic velocity changes in the epicentral region of the 2008 Wenchuan earthquake measured from three-component ambient noise correlation techniques. *Geophysical Research Letters*, *41*, 37–42. <https://doi.org/10.1002/2013GL058682>.
- Lyakhovskiy, V., Ben-Zion, Y., & Agnon, A. (1997). Distributed damage, faulting, and friction. *Journal of Geophysical Research*, *102*, 27635–27649.
- Meier, U., Shapiro, N. M., & Brenguier, F. (2010). Detecting seasonal variations in seismic velocities within Los Angeles basin from correlations of ambient seismic noise. *Geophysical Journal International*, *181*, 985–996. <https://doi.org/10.1111/j.1365-246X.2010.04550.x>.
- Nakata, N., & Snieder, R. (2011). Near-surface weakening in Japan after the 2011 Tohoku-Oki earthquake. *Geophysical Research Letters*, *38*, L17302.
- Niu, F., Silver, P., Daley, T., Cheng, X., & Majer, E. (2008). Preseismic velocity changes observed from active source monitoring at the Parkfield SAFOD drill site. *Nature*, *454*, 204–208.
- Nur, A., & Simmons, G. (1969). The effect of saturation on velocity in low porosity rocks. *Earth and Planetary Science Letters*, *7*, 183–193.
- Obermann, A., Froment, B., Campillo, M., Larose, E., Planes, T., Valette, B., et al. (2014). Noise correlations to image structural and mechanical changes associated with the M_w 7.9 2008 Wenchuan earthquake. *Journal of Geophysical Research*, *119*, 3155–3168.
- Obermann, A., Planes, T., Hadziioannou, C., & Campillo, M. (2016). Lapse-time-dependent coda-wave depth sensitivity to local velocity perturbations in 3-d heterogeneous elastic media. *Geophysical Journal International*, *207*, 59–66.
- Obermann, A., Planes, T., Hadziioannou, C., & Campillo, M. (2018). 4-D imaging of subsurface changes with coda waves: numerical studies of sensitivity kernels and applications to the M_w 7.9, 2008 Wenchuan earthquake, *Pure and Applied Geophysics*, in press.
- Obermann, A., Planes, T., Larose, E., & Sens-Schönfelder, C. (2013). Depth sensitivity of seismic coda waves to velocity perturbations in an elastic heterogeneous medium. *Geophysical Journal International*, *194*, 372–382.
- Peng, Z., & Ben-Zion, Y. (2006). Temporal changes of shallow seismic velocity around the Karadere-Duzce branch of the north Anatolian fault and strong ground motion. *Pure and Applied Geophysics*, *163*, 567–599. <https://doi.org/10.1007/s00024-005-0034-6>.
- Rivet, D., Campillo, M., Shapiro, N. M., Cruz-Atienza, V., Radiguet, M., Cotte, N., et al. (2011). Seismic evidence of nonlinear crustal deformation during a large slow slip event in Mexico. *Geophysical Research Letters*, *38*, L08308. <https://doi.org/10.1029/2011GL047151>.
- Roux, P., & Ben-Zion, Y. (2014). Monitoring fault zone environments with correlations of earthquake waveforms. *Geophysical Journal International*, *196*, 1073–1081. <https://doi.org/10.1093/gji/ggt441>.
- Rubinstein, J. L., & Beroza, G. C. (2005). Depth constraints on nonlinear strong ground motion from the 2004 Parkfield earthquake. *Geophysical Research Letters*, *32*, L14313. <https://doi.org/10.1029/2005GL023189>.
- Sawazaki, K., Sato, H., Nakahara, H., & Nishimura, T. (2009). Time-lapse changes of seismic velocity in the shallow ground caused by strong ground motion shock of the 2000 Western-Tottori Earthquake, Japan, as revealed from coda deconvolution

- analysis. *Bulletin of the Seismological Society of America*, 99, 352–366.
- Schaff, D. P., & Beroza, G. C. (2004). Coseismic and postseismic velocity changes measured by repeating earthquakes. *Journal of Geophysical Research*, 109, B10302. <https://doi.org/10.1029/2004JB003011>.
- Sens-Schönfelder, C., & Larose, E. (2010). Lunar noise correlation, imaging and monitoring. *Earthquake Science*, 23, 519–530.
- Sens-Schönfelder, C., & Wegler, U. (2006). Passive image interferometry and seasonal variations of seismic velocities at Merapi volcano, Indonesia. *Geophysical Research Letters*, 33, L21302.
- Silver, P. G., Daley, T. M., Niu, F., & Majer, E. L. (2007). Active source monitoring of cross-well seismic travel time for stress-induced changes. *Bulletin of the Seismological Society of America*, 97, 281–293.
- Wegler, U., & Sens-Schönfelder, C. (2007). Fault zone monitoring with passive image interferometry. *Geophysical Journal International*, 168, 1029–1033.
- Wessel, P., Smith, W. H. F., Scharroo, R., Luis, J. F., & Wobbe, F. (2013). Generic mapping tools: improved version released. *Eos*, *Transactions American Geophysical Union*, 94(45), 409–410. <https://doi.org/10.1002/2013EO450001>.
- Wu, C., Delorey, A., Brenguier, F., Hadziioannou, C., Daub, E. G., & Johnson, P. (2016). Constraining depth range of S wave velocity decrease after large earthquakes near Parkfield, California. *Geophysical Research Letters*, 43, 6129–6136. <https://doi.org/10.1002/2016GL069145>.
- Wu, C., Peng, Z., & Ben-Zion, Y. (2009). Non-linearity and temporal changes of fault zone site response associated with strong ground motion. *Geophysical Journal International*, 176, 265–278. <https://doi.org/10.1111/j.1365-246X.2008.04005.x>.
- Yamamura, K., Sano, O., Utada, H., Takei, Y., Nakao, S., & Fukao, Y. (2003). Long-term observation of in situ seismic velocity and attenuation. *Journal of Geophysical Research: Solid Earth*. <https://doi.org/10.1029/2002jb002005>.
- Zhao, P., & Peng, Z. (2009). Depth extent of damage zones around the central Calaveras fault from waveform analysis of repeating earthquakes. *Geophysical Journal International*, 179, 1817–1830. <https://doi.org/10.1111/j.1365-246X.2009.04385.x>.

(Received June 14, 2018, revised November 25, 2018, accepted December 5, 2018, Published online December 17, 2018)